1-1-1999

Demonstration of Literal Three-Dimensional Imaging

Cheng Ho

Kevin L. Albright

Alan W. Bird

Jeffrey Bradley

Donald E. Casperson

Miles Hindman

See next page for additional authors

Ho, Cheng, Kevin L. Albright, Alan W. Bird, Jeffrey Bradley, Donald E. Casperson, Miles Hindman, William C. Priedhorsky, W. Robert Scarlett, R. Clayton Smith, James Theiler, and S. Kerry Wilson. 1999. "Demonstration of Literal Three-Dimensional Imaging." Applied Optics 38 (9): 1833–40. doi:10.1364/AO.38.001833.

Demonstration of literal three-dimensional imaging

Cheng Ho, Kevin L. Albright, Alan W. Bird, Jeffrey Bradley, Donald E. Casperson, Miles Hindman, William C. Priedhorsky, W. Robert Scarlett, R. Clayton Smith, James Theiler, and S. Kerry Wilson

In a recent paper a new technique was proposed for remote ranging and topographical mapping by using a system with a single-photon-counting detector and a low-power pulsed laser [Appl. Opt. **35,** 441 (1996)]. We report on the results from the laboratory and the field demonstration of this literal three-dimensional imaging technique. Using a detector system developed at Los Alamos with a commercial pulsed laser and observing from a single remote vantage point, we demonstrate use of this technique in the literal mapping of three-dimensional topography and the probing of a complex scene. With a reasonably short exposure this system can resolve features with height variations as small as 5 cm. © 1999 Optical Society of America

OCIS codes: 110.6880, 040.5160.

1. Introduction

In a recent paper by Priedhorsky *et al.*[1] a technique is described in which a high-resolution photon-counting imaging system is used for remote measurement of the three-dimensional topography of a target scene. This three-dimensional imaging concept is based on the ability to measure, accurately and absolutely, the position and the arrival time for individual photons. Suppose we illuminate a scene with a light source containing a known time signature such as periodic sharp laser pulses and observe remotely with a photon-sensor system that offers both high spatial and time resolution. The detected photons come either from the random background or from the reflection from the scene of the illumination. The background photons have no embedded time signature, whereas the reflected photons from the illumination retain the known time signature. By performing a correlation with the time signature, we can significantly enhance the signal over the background. Use of a narrow-band filter in conjunction with a laser allows us to reduce the background contribution further. In the end we can obtain high-quality three-dimensional (x, y, t) information even in a conventionally low signal-to-background condition. As in a conventional lidar, the arrival time of the photons is translated directly to the range. Combined with the imaging capability of the system, the data acquired with this technique yield the literal three-dimensional profile of the target scene.

As Priedhorsky *et al.* discussed, this technique not only opens many new applications but also offers great advantages over existing sensor systems. In its simplest form this technique permit us to derive the relative topography of solid objects in the scene from a single remote vantage point. A large-area high-accuracy survey of ground topography can be achieved from an airborne platform by using a low-power laser, which would be a great advantage over the existing scanning lidar altimeter. Furthermore the scattering property and distribution of a complex three-dimensional structure can be probed with this system. For example, this technique can be used to study the multiple-scattering and radiation transfer properties of a cloud.[2] Another application is to the measurement of the distribution of plant leaves as three-dimensional suspended objects. Issues such as biomass in a forest or plant health could be addressed by such measurements.

Since mid-1997 an end-to-end system with the capabilities needed for this literal three-dimensional imaging technique has been in operation. To demonstrate this novel three-dimensional imaging technique fully, we conducted a number of experiments both in the laboratory and in the field. The ability and accuracy of three-dimensional imaging depends primarily on the available photon statistics and only secondarily on the absolute distance to the target scene. In this paper we report the results of two experiments at two different observing distances

The authors are with the Los Alamos National Laboratory, Mail Stop D436, Los Alamos, New Mexico 87545.

Received 5 June 1998; revised manuscript received 26 October 1998.

0003-6935/99/091833-08$15.00/0

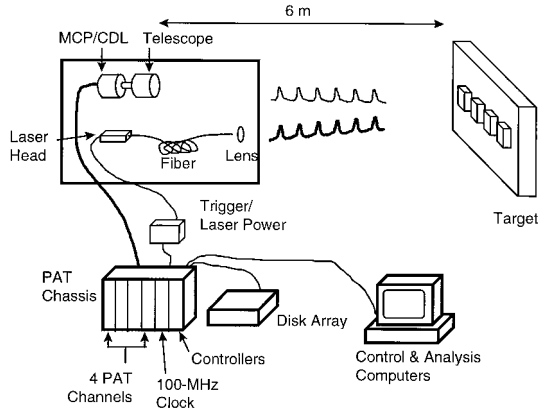

Fig. 1. Schematic of the laboratory experimental setup. The entire experiment is contained in a 24-ft (7.3-m)-long dark laboratory.

Fig. 2. Styrofoam target used in the laboratory experiment.

when the same low-power laser is used, a laboratory experiment in which an artificial target is observed from a distance of 6 m, and a field experiment in which a natural scene is observed from a distance of 50 m. These results quantitatively demonstrate the concept of remote literal three-dimensional imaging.

The organization of this paper is as follows: In Section 2 we discuss the laboratory experiment, data processing and analysis, and results. To help explain the concept, we have adopted a pedagogical approach in the analysis in Subsection 2.B. In Section 3 we describe the field experiment and the results. In Section 4 we give a summary and discussion.

2. Laboratory Experiment and Results

A. Experimental Setup

The experiment consists of the following major components: a dark laboratory, a pulsed laser as the illumination system, the target, light-collecting optics, and, most important, the sensor system with a microchannel plate (MCP)/crossed delay line (CDL) detector with pulse absolute timing (PAT) electronics. We describe the characteristics of individual components as follows:

Laboratory. The experiment was conducted in a dark laboratory with an overall length of ~7 m. The laboratory can be made relatively dark with some minor light sources. With a narrow-band filter as described below, the ambient light was reduced to a manageable level. An optical table was located at one end of the room where the illumination and the observing subsystems were attached. The target was placed at the other end of the laboratory at a distance of ~6 m from the sensor system. A schematic of the experiment is shown in Fig. 1.

Target. A target was constructed from a block of 5-cm-thick Styrofoam (open cell expanded polystyrene foam). Four block letters, LANL, with a line thickness of approximately 1.5–2 cm, were carved from the Styrofoam block. The four letters were glued to a 30 cm × 50 cm Styrofoam block of the same 5-cm thickness. The base Styrofoam block was attached vertically to the wall. Figure 2 shows the target where the letters can be distinguished based on the shadows.

Illumination system. As described by Priedhorsky *et al*. this technique requires active illumination with known timing characteristics. For this experiment we use a Hamamatsu PLP-01 solid-state laser that is externally triggered at 1.5625 MHz and synchronized to the reference 100-MHz clock of the PAT electronics described below. The laser head emits 83-ps light pulses at 655 nm with a peak power of 54 mW: At a 640-ns pulse period the average power is ~7 μW. The laser output beam shape is highly asymmetric. To achieve a more uniform illumination, we couple the laser to a 120-μm-diameter 7-m-long multimode optical fiber. The divergence of the beam at the exit of the optical fiber is ~45 deg. A lens placed in front of the fiber exit helps concentrate the light on the target area.

Light-collecting optics. We use an Orion Maksutov–Cassegrain 500-mm $f/5.6$ telescope to collect the light. The collection optics and the illumination system are roughly collocated on the same optical table. An imaging-quality narrow-band filter centered at 655 nm with a 10-nm bandpass is placed behind the telescope and immediately in front of the detector. The target block is focused and centered on the detector's active sensing area.

MCP/CDL/PAT. The MCP/CDL detector is a hermetically sealed vacuum tube made by Photek, Ltd. (UK) under a contract from the Los Alamos National Laboratory. The tube uses S-20 photocathode material for light sensing. Through a triple stack of 40-mm-diameter MCP's arranged in a chevron fashion (a Z-stack) each excited photoelectron is intensified by a factor of $\sim 10^7$. The resulting charge cloud is read out by a CDL anode with two orthogonal layers of helical conducting wires.[3,4] Each layer of wire has two ends, and each photon event generates electrical pulses at all four ends. The position and time of the photon event are determined by measuring the relative and the average pulse arrival time of the four pulses from the same photon event. This

measurement is achieved by acquiring the data through a fast timing system, the PAT electronics, that contains four channels referenced to a common clock. Each channel is triggered independently by the four readouts of the CDL anode. The current PAT system is implemented on industry-standard Versa Module Eurocard architecture and contains four separate PAT channels commonly referenced to a stable 100-MHz clock. Each PAT channel contains custom analog-to-digital circuits that measure the absolute timing of individual electrical pulse with a resolution of 2.44 ps. The independent measurement of the arrival time of the four pulses permits us to reconstruct the photon event through an algorithm based on coincidence constraint, discriminating between two simultaneous events.

To date we have achieved the following performance in the laboratory. The best FWHM of a point source measured through the end-to-end MCP/CDL/PAT system is 60 μm. The timing accuracy for each photon is ~200-ps rms or 420-ps FWHM. We expect the current implementation to offer a linear response to a random count rate as high as $\sim 10^6$ counts/s before significant event degradation occurs owing to coincidence. For the literal three-dimensional (3D) imaging field and laboratory experiments the system has slightly degraded spatial and timing performance from the numbers above. As we continue to improve the system, we expect a point-source FWHM of better than 30 μm, an absolute timing FWHM of ~100 ps, and a maximum count rate of 5×10^6 counts/s. A more detailed description and performance of the MCP/CDL/PAT system are given elsewhere.

The experiment was conducted in the dark conditions described above. To control the data acquisition and perform a quick-look analysis, we used two notebook computers in the same laboratory. The detector has a dark count rate of ~600 counts/s over its entire active area. Through the narrow-band filter the ambient light, which included reflected light from two computer screens, contributed another ~600 counts/s. The reflected laser light contributed ~1200 counts/s. With an overall count rate of ~2400 counts/s the system's capability was significantly underutilized. A number of data sets were acquired in the same conditions at 240 s of exposure each. Data were stored as a raw pulse-arrival-time series from each channel for post-factum processing and analysis. We note that the same exposure can be performed in less than 1 s with a laser of 3-mW average power that would yield approximately 5×10^5 counts/s.

B. Data Processing, Analysis, and Results

Taking at face value the breakdown of various contributions to the count rate, one would conclude that the signal-to-background ratio of the laser illumination in the data set is 1:1. In normal circumstances such a signal-to-background ratio would contain limited useful information. However, the high-accuracy timing information for each photon coupled with usage of the pulsed laser permits us to perform a straightforward timing analysis to separate the signal from the background. Through the timing analysis the background is effectively removed. The data processing and analyses are performed by the following standardized steps:

(1) Raw data are processed into photon events.
(2) Photon events are time analyzed to establish correlation of the laser return photons.
(3) Random background is reduced through phase selection.
(4) Topography information is calculated from the data.

Step 1: Photon-event construction. The raw timing data sets are processed through the step of photon-event construction based on a coincidence algorithm that is a key aspect of the MCP/CDL/PAT system. With the current implementation, each exposure will yield four associated data sets, each containing an independent time series, $\{x1\}$, $\{x2\}$, $\{y1\}$, and $\{y2\}$. Each of the time series has a high precision and a high dynamic range: The time is recorded as an integer in units of 2.4414 ps with a dynamic range of 58 bits. Out of the four independent time series, valid photon events are constructed by

$$x = x1 - x2, \tag{1a}$$

$$y = y1 - y2, \tag{1b}$$

$$t = (x1 + x2 + y1 + y2)/4, \tag{1c}$$

where the coincidence constraint must be satisfied for each event:

$$d = |(x1 + x2) - (y1 + y2)| < \delta. \tag{1d}$$

The width of the coincidence widow δ is small, currently measured to be approximately a few hundred picoseconds. This stringent constraint offers the capability of discriminating between two simultaneous but not collocated photon events, leading to an effective detector dead time of a few tens of nanoseconds. This step yields a list of photons recorded as the event position and the time (x, y, t) at the detector's sensing surface. An analysis of high-precision timing can be performed over the entire exposure. In the remainder of this paper, we discuss the analyses and results of one 4-min exposure.

We extract the data set that contains 256×256 pixels with each pixel covering an area of ~150 μm square on the detector's surface. This data set maps a pixel of an 1.8-mm square at the target with the field of view (FOV) covering ~45 cm^2. Figure 3(a) shows a negative image constructed from the full data set. The circular area is defined by the detector's active area. The four corners of the FOV in the data space, devoid of photons, do not map to the detector's active area. The edges of the detector's circular active area, on the other hand, have been truncated in this format. There are several notable

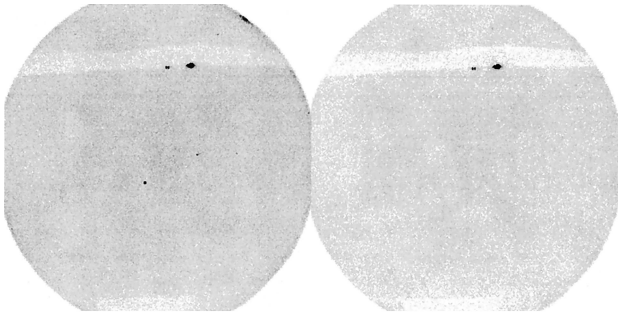

Fig. 3. Images of the target scene from the laboratory experiment. The intensity map is shown as the negative, i.e., darker pixels contain more counts. (a) Image constructed from the total data set. The features are described in the text. (b) Image constructed from the phase-culled data set that contains approximately half of the number of photons of the image in (a). In addition to being dimmer than (a), (b) also lacks the spots at the center and the upper right corner of the FOV. The spots are randomly distributed in time and suppressed by phase culling.

features in this image: (1) The two dark stripes (light intensity corresponding to low counts) at the top and bottom are the black optical tapes used to attached the Styrofoam block to the wall. (2) The two bright spots in the upper half of the image are caused by specular reflection of the laser from a metallic electrical wall panel that was not fully covered by black tape. (3) The bright spots in the middle of the FOV and the upper right corner are hot spots that have developed inside the tube. Unlike Fig. 2, one cannot see the letters LANL in Fig. 3 through either intensity contrast or shadow.

Step 2: Time analysis. As described by Priedhorsky *et al.*, the fact that the target scene was illuminated by a source with a known time signature permits us to separate the laser return photons from the random background. The time–random background includes the intrinsic detector dark count, the ambient light, and the hot spots in the detector. These background photons have a random arrival time and no correlation with the laser pulse period. In contrast, the returned laser photons retain the time signature of the pulsed laser. To distinguish photons with a random and a periodic time signature, we construct a secondary photon list in which the time for each photon is the phase of the photon's arrival time relative to the periodicity. Specifically, the secondary photon list (x, y, t') is related to (x, y, t) by

$$t' = (-t + \mathrm{d}t_F + \mathrm{d}t_I)\text{modulo } P, \tag{2}$$

where $P = 640$ ns. Without loss of generality, we intentionally use the negative value of t to calculate t' so that the calculated phase maps directly to topography as if we are looking down from the top: Photons with larger t' are reflected from a location closer to the observer. In Eq. (2) we introduce two correction terms, $\mathrm{d}t_F$ and $\mathrm{d}t_I$, to remove various sources of curvature in the observed field. First, as described

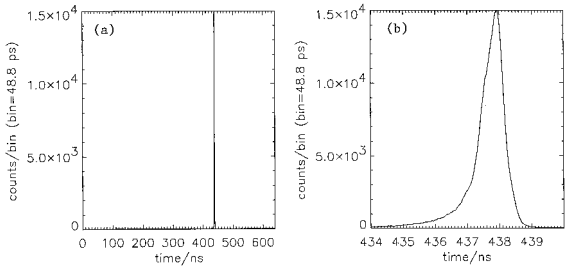

Fig. 4. Phase distribution of the photon list: (a) Overall distribution of the calculated phase from 0 to 640 ns. (b) Dominant feature at 438 ns in greater detail.

by Priedhorsky *et al.*, geometry dictates that photons reflected from different parts of the FOV travel different distances between the illumination source and the detection. To correct this field curvature, we apply a correction factor,

$$\mathrm{d}t_F = T_F[\sec(\theta) - 1], \tag{3}$$

where θ is the angle of the photon's registered position relative to the center of the FOV and T_F is the round-trip time for photons detected at the center of the FOV, which we have taken to be 40 ns across a distance of 6 m. Second, photons emerging from the optical fiber at different angles have different propagation path lengths through the fiber. This difference leads to a strong dependence of timing on the exit angle. In a way the laser pulse is broadened. To correct for the curved illumination front, we apply a second correction factor:

$$\mathrm{d}t_I = T_I[\sec(\kappa\theta) - 1]. \tag{4}$$

The normalization factor T_I is taken to be 35 ns for the propagation time of the photons along the fiber, after the fiber's index of refraction is taken into account. The factor κ is introduced to account for the light-concentrating lens. For this analysis we take $\kappa = 2$. In this formalism we are making the implicit assumption that the illumination and the observing system are collocated. As discussed below the quality of the results indicates that the collocation assumption is reasonable. Figure 4(a) shows the phase distribution over the full range of 640 ns for the entire data set that contains ~571,000 photons. Most of the phase range contains an average of ~24 counts/48.8-ps phase bin. This distribution is obviously dominated by a sharp feature at 438 ns, the highly correlated laser return bearing the pulse signature.

Step 3: Phase culling. With the sharply peaked phase distribution near 438 ns we construct a culled data set that contains only those photons with a phase in the range of 434–440 ns. They are predominantly returned laser light. The image from the culled data set is shown in Fig. 3(b). The main difference between the Figs. 3(a) and 3(b) is the absence of hot spots at the center and the edge of the FOV that have no time signature. Figure 4(b) shows the distribution of the phase-culled data set contain-

ing ~288,000 photons. We estimate that the random background contributes ~2900 photons within the 6-ns phase range. Thus the signal-to-background ratio in the culled data set is ~100:1. The peak is fully resolved with a FWHM of 680 ps, slightly greater than, yet consistent with, the best achieved time accuracy discussed above. There is no strong evidence of any complex structure in Fig. 4.

Step 4: Topography extraction. The phase-culled data set is processed by the simple topography-determination algorithm outlined by Priedhorsky *et al*. We constructed a local phase distribution around each pixel based on the photons falling within an $n \times n$ pixel region centered around the pixel in question. For this analysis we take $n = 3$. The median of the localized phase distribution is designated as the pixel's range: When we multiply the median phase by a factor of $c/2$, with c being the speed of light, the median phase maps directly to the topographical height. Figure 5 shows the calculated topographical map: Figures 5(a), 5(b), and 5(c) show the topographical map as an intensity map, contour plot, and surface plot, respectively. It is obvious that we have resolved the 5-cm-height separation between the LANL letters and the solid Styrofoam block. The flatness of the topographical images, most visible in Figs. 5(a) and 5(b), indicates the absence of a significant residual field curvature and confirms the validity of various assumptions and correction terms used in the analysis.

To characterize the system performance further, we plot the distribution of calculated heights for the ensemble of pixels in Fig. 6. The distribution is clearly multimodal. Three broad yet distinct peaks are seen near 20, 25, and 30 cm, which we identify as the wall, the flat surface of the solid Styrofoam base, and the letters LANL, respectively. The height difference matches the thickness of the building material of the target, standard 2-in. (5-cm)-thick Styrofoam blocks available in local hobby stores. In this figure pixels with fewer than two counts, including the four corners in the images shown in Fig. 3, have been assigned a height of 17 cm, shown as the sharp peak at the said location.

We now compare these results with the theoretical expectation. The average count per pixel in the culled data set is ~4. The local phase distribution used to calculate the height would typically contain 36 counts from 9 pixels. Given the high signal-to-background ratio of the culled data set, it is reasonable to assume that the distribution follows normal statistics dictated by the single-photon timing accuracy. Suppose we use the 680-ps FWHM shown in Fig. 3 as the underlying time accuracy for individual photons. We estimate that the mean/median can be determined to an accuracy of ~680 ps/$(36)^{1/2}$ ~ 110-ps FWHM. This FWHM corresponds to an estimated FWHM for the distribution of a calculated height of ~1.7 cm. Literal measurement around the peak at 25 cm in Fig. 6 gives a FWHM of ~2.8 cm. Keeping in mind that we have applied two correction factors and that the topography-extraction algorithm is not truly local, we consider this height-determination accuracy to be in reasonable agreement with the simple theoretical estimate. This agreement again confirms the validity of the time-correction terms used in Eqs. (3) and (4). For exam-

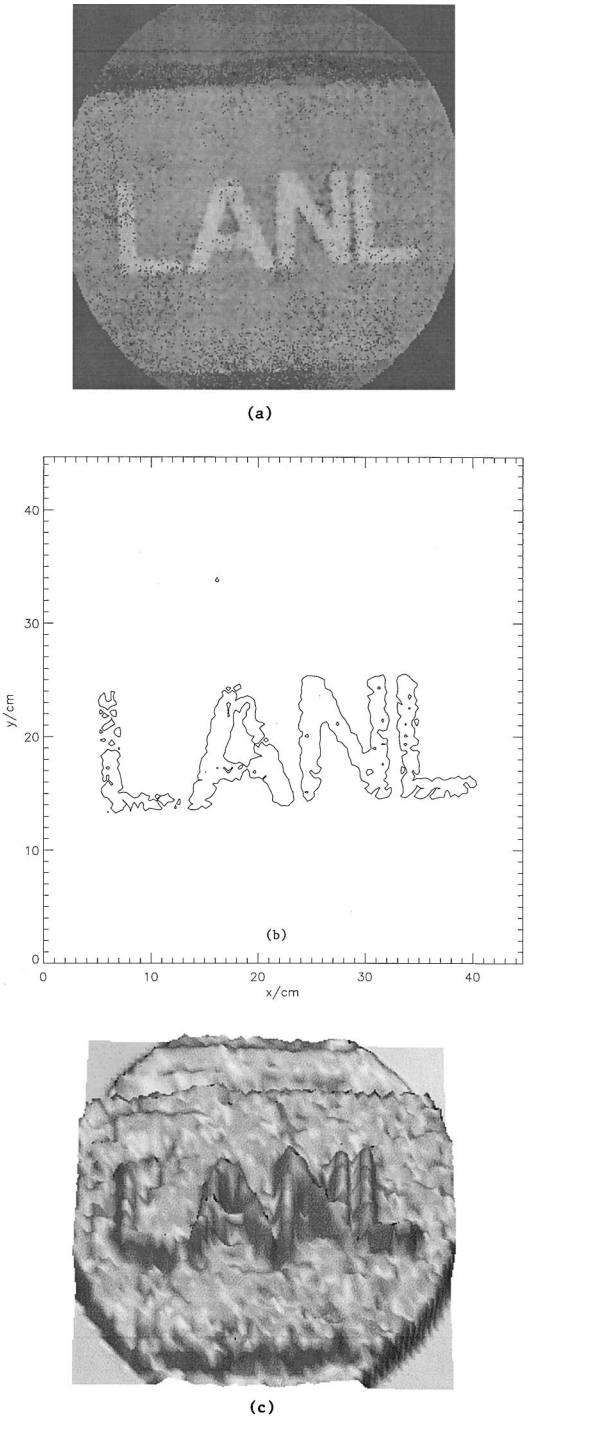

Fig. 5. (a) Calculated topographical map of the target as a positive intensity map. Brighter pixels have greater height or are closer to the observer. (b) Contour map of the calculated topography. To reduce confusion, only one contour level at 27.5 cm (see Fig. 6) is imposed. (c) Calculated topography shown as a surface plot viewed from a slightly oblique angle. In this visualization a lighting effect is used to form a shadow.

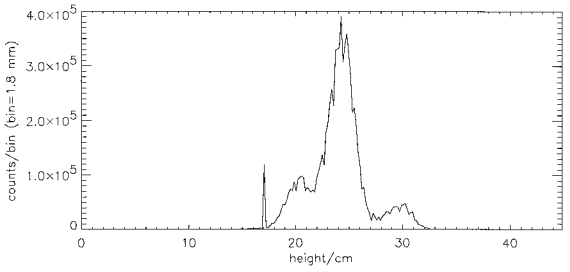

Fig. 6. Distribution of the calculated height, which is clearly multimodal. The features at 20, 25, and 30 cm are the wall, the solid Styrofoam block, and the letters LANL, respectively. The sharp feature at 17 cm is the assigned height of the pixels with less than two counts. These are the dark pixels shown in Fig. 5(a).

ple, if these corrections were not applied, the curved field would incur a discrepancy at the edge of the FOV of the order of 270 ps or 4 cm, which would have been readily apparent in the height map or distribution.

3. Field Experiment and Results

A. Experimental Setup

The field experiment follows the same principle and setup as the laboratory experiment. Below we briefly review the field experiment setup with emphasis on the differences between the field and the laboratory experiments.

Field setup. We conducted the field experiment in a local canyon. The entire illumination and observing system was located in a self-contained recreational vehicle parked on a paved road in the middle of the canyon. The vehicle was ~50 m from the foot of the canyon wall where the target was situated. The experiment was performed in a moonless condition.

Target. In addition to the natural scene at the foot of the canyon wall, we placed a 3-ft (91-cm) cubical wooden box at the target scene. The box was painted in a black-and-white checkerboard pattern as shown in Fig. 7. To simplify the analysis and the data interpretation, we covered the box with solid-yellow carpet during the experiment. Figure 7 clearly shows that the box was located on sloped ground and leaning slightly forward.

Illumination. We used the same pulsed laser externally triggered at 1.5625 MHz. For this experiment we chose to use directly the beam out of the laser head without the intervening fiber. As a result, illumination of the scene was not uniform but without illumination curvature [see Eq. (4)].

Optics and MCP/CDL/PAT. These subsystems were essentially identical to the configuration used in the laboratory experiment.

Experiment. Data were acquired following the standard procedures. Across the entire detector area the detector dark count was ~600 counts/s, and the scene contributed ~800 counts/s through the narrow-band filter in the moonless condition. The laser return accounted for ~1500 counts/s.

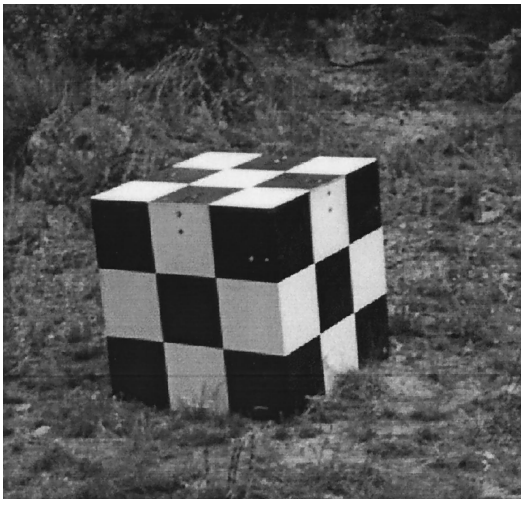

Fig. 7. Wooden-box target [3-ft (0.9-m) cube] that was used for the field experiment. A solid-yellow carpet covered the entire box during the experiment. Note the slope of the ground and the forward lean of the box.

B. Analysis and Results

In this subsection we describe the results of a 200-s exposure taken in the field experiment. The data processing follows the standardized procedures described in Subsection 2.B with the exception that we have not applied the topography-determination algorithm.

After constructing the photon events, we performed the time analysis following Eq. (2). For this data set the illumination-front correction term dt_I was not applied because we used the laser output directly in the experiment. Photons from an ~3.8-m-square region at the target location are extracted from the data set with 256 × 256 pixels in the spatial dimension. This data set contains ~494,000 photons. The phase distribution for 640 ns is shown in Fig. 8(a). Compared with Fig. 4(a), Fig. 8(a) exhibits much more complicated structures. The features in the range of 250–350 ns (corresponding to a distance range of ~15 m) can be identified as various foreground objects. Among the foreground objects were tall weeds in the canyon floor that contributed to the lower portion of the FOV. In this paper we concentrated on the time period between 220 and 245 ns. The phase distribution is shown in Fig. 8(b). The

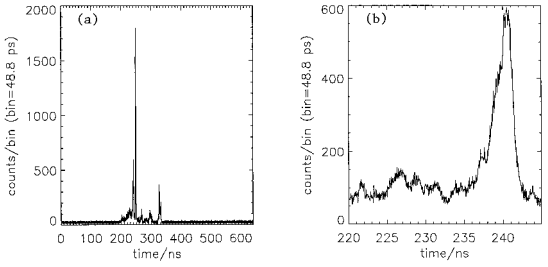

Fig. 8. Phase distribution of the field experiment data set: (a) the full 640-ns range in which complex structures can easily be seen and (b) the range between 220 and 245 ns.

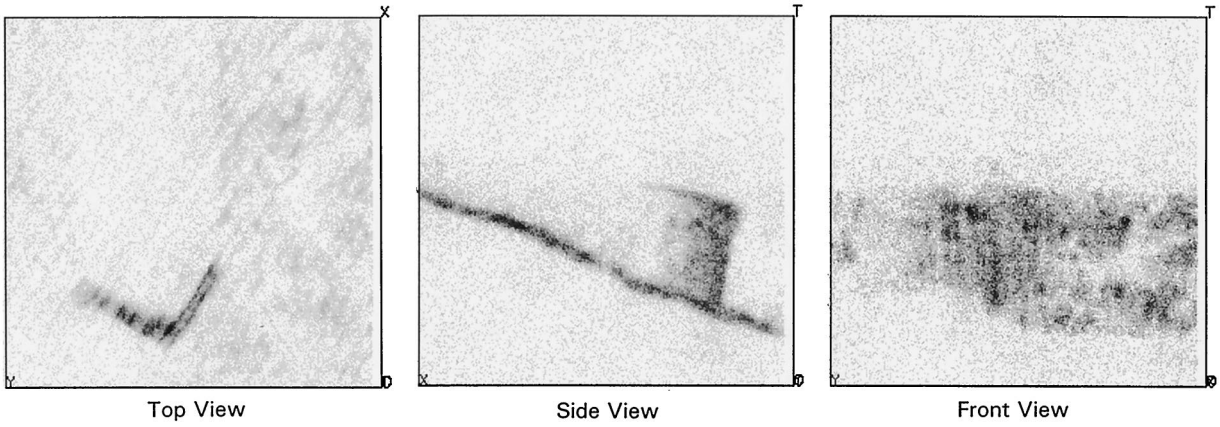

Fig. 9. Three-dimensional data box as negative images project from different viewing angles. The 3D box is labeled as follows: $+T$ axis is up, $+Y$ axis is to the left as viewed from the front, and $+X$ is along the line of sight away from the observer. See text for a more detailed discussion.

phase-culled data set contains 74,000 photons with ~10,000 photons from the random background.

The phase-culled data set contains photons distributed in a volume with a size of ~3.8 m on each side. The resolution in each dimension is 1.5 cm or better. This resolution permits us to perform direct visualization of the data. Figure 9 shows separately the projected images of this data cube along the three axes: the front, top, and side views.

In the front view we can distinguish the box in the lower left quadrant after consulting the other views. The two front surfaces are more prominent than the top surface because of the more favorable reflection angle. This view has a bandlike structure that is understood as follows. Because of the sloped ground, foreground and background objects cover the lower and the upper portion of the image, respectively. The selection of a viewing depth of 3.8 m excludes photons reflected from foreground and background objects, leaving only those photons within the right depth range to contribute to the image in a band.

The dominant feature in the top view is the V pattern in the lower left corner that is the projection of the two front surfaces of the box. The V pattern has a finite width estimated to be ~1.5 ns (or 22 cm). This width is greater than the FWHM of a single-photon timing distribution, estimated above to be ~680-ps FWHM in field operation conditions. Close inspection reveals that this width is dictated by the forward lean of the box on the sloped ground, which is easily seen in the side view as well as in Fig. 7. In this view we can also see a void of photons behind the box. This void is the shadow of the laser illumination due to blockage by the box.

The side view clearly shows the sloped ground and the restricted height range due to the selected depth range. One can see the variation of the sloped ground. In addition there is a diffuse distribution of photons above the ground that is the result of reflection of the ground vegetation in the scene as seen in Fig. 7.

The three views show the power of this technique. Data generated by this system literally map the 3D structure of the target scene, which can be directly visualized without extensive and extraneous data processing.

4. Discussions and Summary

In these experiments the phase difference between the laser pulse and the photon time series was arbitrarily fixed for each data set. Except for the correction term dt_F, the relative topographical map is derived without explicit determination of the absolute distance. As discussed in a Subsection 2.B, the height-determination accuracy can be predicted by photon statistics, which are determined by laser power, distance, and exposure time. Bearing in mind that these experiments used a laser of low power and significantly underutilized the capabilities of the MCP/CDL/PAT system, we do not foresee any difficulty in achieving the system performance discussed by Priedhorsky *et al*.

Knowledge of the absolute distance is necessary to apply the field curvature compensation factor correctly in Eq. (2). As stressed by Priedhorsky *et al*., built in to this concept is a ranging ambiguity of $cP/2$ (96 m for the 640-ns pulse period). For an observing distance smaller than $cP/2$ it is straightforward to determine the absolute phase difference of the illumination and the laser return. For measurements with a distance greater than $cP/2$ we can either employ a conventional ranging system to supply the information or perform self-consistent algorithmic determination of the range by examining the observed field curvature.

A comparison between the raw image (e.g., Fig. 3) and the topographical image (e.g., Fig. 5) demonstrates the power of this technique: This technique remotely measures the literal 3D profile of the target with a short exposure from a single vantage point. Compared with existing remote 3D probing schemes such as synthetic aperture radar and scanning lidar,

this system offers the following advantages: a low-power eye-safe laser, low weight and power requirements as described by Priedhorsky *et al*., no moving parts or stringent alignment requirements, simultaneous coverage over a wide area in short exposures, and data that are literally three-dimensional and require no extraneous data processing.

As discussed above the essence of this technique is measurement of the 3D distribution of return photons from a scene under directed illumination. The distribution of the return photons maps literally to the reflecting or backscattering elements in the observed scene. Although the experiments reported in this paper were performed for solid targets with contiguous surfaces, it is straightforward to apply this technique to measuring reflecting objects suspended in three dimensions or even more complex 3D structures.

To summarize, we have demonstrated the concept of imaging the 3D profile of a remote target by using a single-photon-counting detector and active illumination. We envisage many applications for this new technique.

This research was performed under the auspices of the U.S. Department of Energy. C. Ho thanks Lauren and Karen Ho for their assistance with the construction of the Styrofoam target.

References

1. W. C. Priedhorsky, R. C. Smith, and C. Ho, "Laser ranging and mapping with a photon-counting detector," Appl. Opt. **35,** 441–452 (1996).
2. A. B. Davis, C. Ho, and S. P. Love, "Off-beam (multiply-scattered) lidar returns from stratus. 2: Space–time measurements in a laboratory simulation," in *Proceedings of the 19th International Laser Radar Conference*, U. Singh, S. Ismail, and G. Schwemmer, eds. (NASA Center for Aero-Space Information, Annapolis, Md., 1998) pp. 55–58.
3. M. B. Williams, S. E. Sobottka, and J. A. Shepherd, "Delay line readout of MicroChannel Plates in a prototype position-sensitive photomultiplier tube," Nucl. Instrum. Methods Phys. Res. **A302,** 105–112 (1991).
4. M. H. Baron and W. C. Priedhorsky, "Crossed delay line detector for ground and space based applications," in *EUV, X-Ray and Gamma-Ray Instrumentation for Astronomy IV*, O. H. Siegmund, ed., Proc. SPIE **2006,** 188–197 (1993).